J. Mech. Phys. Solids 146 (2021) 104187

Contents lists available at ScienceDirect

Journal of the Mechanics and Physics of Solids

journal homepage: www.elsevier.com/locate/jmps

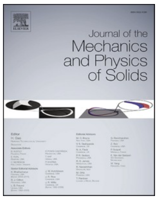

Mechanics Based Tomography (MBT): Validation using experimental data

Sevan Goenezen *[,a,d], Baik Jin Kim [a], Maulik Kotecha [a], Ping Luo [b], Mohammad R. Hematiyan [c]

[a] *Mechanical Engineering, Texas A&M University, College Station, TX 77843, United States*
[b] *Yale Center for Research Computing, Yale University, New Haven, CT 06520, United States*
[c] *Mechanical Engineering, Shiraz University, Shiraz 71936, Iran*
[d] *Engineering Solutions and Quality Products, LLC, Texas, United States*

ARTICLE INFO

Keywords:
Solid mechanics
Tomography
Digital image correlation
DIC
Inverse problems
Elasticity imaging
Non-destructive material characterization
Incomplete data
Non-destructive testing

ABSTRACT

Tomography based imaging is used in various disciplines with the most widely known as computed tomography (CT). In general, they have in common that a signal is measured on the specimen's surface and at multiple locations to reconstruct some type of a material property distribution using application specific constitutive equations. In this paper and for the first time with experimental validation, a novel tomography approach is successfully introduced based on the mechanics of solids. It utilizes the equations of equilibrium at its core embedded in an optimization framework to control the ill-posed nature of these problems. Measured signals are deformation fields obtained from a digital image correlation system with photo cameras. This work demonstrates the potential of mechanics based tomography (MBT) on a composite silicone material. This work encourages to investigate MBT as a breast tumor screening tool to visualize tumors based on their stiffness contrast. Another long-term goal could be to investigate the use of this methodology as a non-destructive testing tool for civil engineering structures such as bridges. Finally, this new methodology could potentially be miniaturized with stereoscopes and extended to map the material property distribution at the microstructure, e.g. grain length-scale.

1. Introduction

Tomography has been developed in various disciplines and the most widely known is the computed tomography (CT) that has broad applications in the medical field. CT scans also find applications in engineering to visualize the interior structure of engineering materials pertaining to detecting defects (Vicente et al., 2017; Yu et al., 2016). Ultrasound tomography is still at its infancy, but has dramatically improved in recent years. However, ultrasound tomography is confined to soft tissues (Wiskin et al., 2017), since acoustic signals do not penetrate deep into hard tissues such as bones. The heat equation has been mapped for its thermal conductivity utilizing surface temperature measurements (Fan et al., 2017; Hematiyan et al., 2015). In Santos et al. (1991) electrostatic surface measurements of voltage potentials were used to non-destructively detect cracks with respect to their location and size in an electrically conducting material (Santosa and Vogelius, 1991). Nondestructive crack detection has also been pursued in a theoretical work using eigenfrequency measurements (Tanaka and Yamagiwa, 1989). In order to obtain a unique solution, the authors in Tanaka and

---

* Corresponding author.
E-mail address: sevangoenezen@gmail.com (S. Goenezen).

https://doi.org/10.1016/j.jmps.2020.104187
Received 11 April 2020; Received in revised form 1 October 2020; Accepted 10 October 2020

Yamagiwa (1989) used multiple eigenfrequencies. Tomography has also been developed in geological sciences, where wave motion from earthquakes or active sources were utilized to image subsurface geological features including fault lines (Roecker et al., 2010; Zheglova et al., 2012).

Tomographic inversion in solid mechanics is ongoing research and started a couple of decades ago with the goal to map the interior mechanical property distribution from surface displacements and forces or tractions. In Schnur and Zabaras (1992), the authors performed a theoretical study to calculate the size of an inclusion and their elastic properties for an isotropic, linear elastic material. The authors therein assume that the domain has only two homogenous regions, the background and the inclusion, which is of circular shape. With these assumptions, the unknowns in the inverse problem are the Young's modulus of background and inclusion, the x-y coordinates of the inclusion center and the radius of the inclusion. Thus, the total number of unknowns reduces to 5. In a theoretical study in Hajhashemkhani et al. (2018), the elastic properties were recovered for a hyperelastic material with model uncertainties in boundary conditions on some parts of the boundary. Tomographic inversions with experimental data were attempted in Van Houten et al. (2011) using time harmonic displacement measurements on silicone phantoms with embedded inclusions. One inclusion was spherical and the other was cylindrical. Here, the number of unknowns were reduced to 3: stiffness of the matrix, the inclusion, and the location of the interface of inclusion to matrix. Olson et al. (2019) constructed a gelatin with an inclusion, to represent a breast with a cancerous tumor. Local force-displacement measurements all around the specimen were collected and used in a minimization scheme using genetic algorithms to reconstruct the stiffness distribution. The authors therein meshed the domain with finite elements with each element having a binary choice of being healthy (Young's modulus of 2.3 kPa) or cancerous (Young's modulus of 18.5 kPa).

Recently, the authors of this paper conducted theoretical studies to demonstrate feasibility of tomographic inversion in solid mechanics to visualize the interior stiffness distribution from synthetic surface displacements (Luo et al., 2018; Mei et al., 2016; Mei et al., 2017). A major difference of this work to the research above is that we have not made any significant assumptions about the distribution of the stiffness property as it may not be known in practical applications. The only assumption we made on the shear modulus distribution was the range of the solution, which was chosen to be quite large. We defined a continuous C^0 distribution of the shear modulus via nodal unknown shear moduli on finite element mesh nodes. Thus, the total number of unknowns in our problem formulation is equal to the total number of finite element mesh nodes. Synthetic displacement measurements were obtained by solving boundary value problems with finite element methods (Reddy, 2005; Reddy, 2013). Since displacement measurements in experiments are noisy, we added varying levels of noise to the synthetic displacements. These data sets were used to minimize an objective function with an embedded regularization term for the unknown nodal shear moduli subject to the constraints of the boundary value problems.

The theoretical studies in our prior publications (Luo et al., 2018; Mei et al., 2016; Mei et al., 2017) were highly encouraging and have motivated this work using experimental data sets. In this paper, we demonstrate feasibility of this method with surface displacement measurements on a silicone-based composite utilizing a digital image correlation system with regular camera resolution. We term this methodology for obvious reasons "Mechanics Based Tomography" or "MBT".

2. Methods

For the *verification* part of this study, we create synthetic surface displacements by solving boundary value problems using finite element methods. The resulting surface displacements are then augmented with noise and used as the "measured" surface displacements to perform the tomographic inversion in solid mechanics. The same problem domain was utilized for the *verification* with synthetic data and experimental *validation* part and is described in the following.

For the *experimental validation*, a cube with dimensions of 70 mm × 70 mm × 70 mm and embedded with two cylindrical inclusions of 10.5 mm and 14.0 mm radii were manufactured using silicone rubber materials. A mold was made of acetal copolymer plastic material and used to create the composite sample shown in Fig. 1(a) and (b). EcoFlex 00-30 and EcoFlex 00-50 (Smooth-On, Inc.) were used for the background and inclusion materials, respectively. Each of these EcoFlex materials were supplied as two parts and were mixed according to manufacturer's specification of equal parts. Afterwards, black Silc-Pig color was added to each mixture to color the sample black.

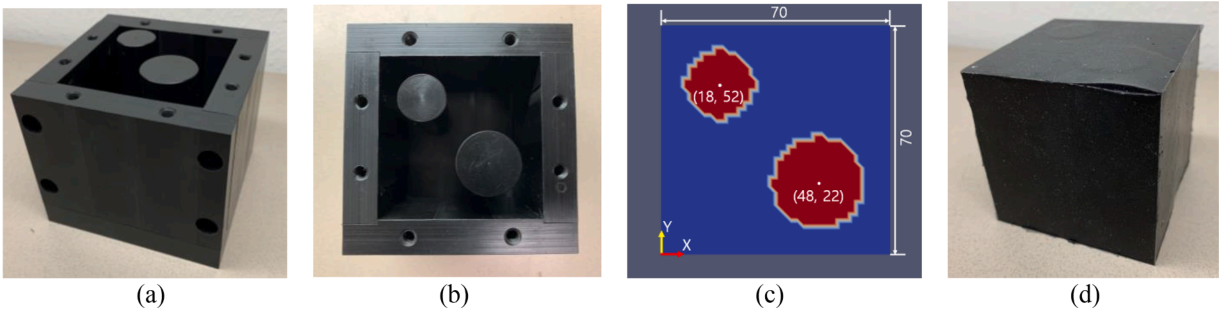

(a) (b) (c) (d)

Fig. 1. (a) Mold with matrix made of silicone rubber material in three-dimensional view; (b) top view; (c) dimensions of the composite silicone cube from the top marked in the finite element model; (d) final composite cube (inclusions not visible).

More details on sample production: the EcoFlex 00-30 solution was mixed with black pigment for 3 min and then placed into a vacuum chamber for 3 min to eliminate any entrapped air forming in the mixture. Then the liquid mixture was dispensed into the mold shown in Fig. 1(a) and (b). The mixture was poured around two rigid cylinders to create the matrix with voids for the inclusions. The two cylinders were removed after twenty-four hours when the background material solidified, followed by pouring EcoFlex 00-50 solution into the voids to create the stiffer inclusions. Curing at room temperature was allowed for about twenty-four hours followed by post curing of the sample in a heated chamber at 80 °C for two hours and 100 °C for one hour. The sample was then removed from the hot chamber to cool to room temperature with the final sample shown in Fig. 1(d). The coordinates of the center of the smaller inclusion and larger inclusion are (18.0 mm, 52.0 mm) and (48.0 mm, 22.0 mm), respectively, with the coordinate system's origin on the bottom left corner shown in Fig. 1(c).

The same EcoFlex materials discussed above were used to construct homogeneous samples to determine their mechanical properties from uniaxial tensile tests. The homogeneous specimens were prepared with dimensions of $10 \times 2 \times 0.3$ cm for height × width × thickness. In order to prevent the sample from slipping between grips, small wooden pieces were glued to the sample ends. The uniaxial tensile tests were performed at room temperature with an INSTRON 5567 machine with wedge action grips. The load cell has a capacity of 5 kN and an accuracy of 0.5% for loads as low as 1/1000th of the maximum capacity. We operated slightly below the above-mentioned recommended limit. The loading was displacement controlled at a deformation rate of 1 mm/min, sufficiently slow to avoid viscoelastic effects. The stress-strain response for the inclusion and background materials are shown in Fig. 2(a).

From the slope of the curves, we determined the Young's modulus of the inclusions to be approximately 1.4 times larger than their background material. We also observed that the stress-strain curves of both materials are nearly linear, thus material nonlinearity is insignificant even for large strains of up to 10% for these materials. Assuming that the silicone material is incompressible, the target shear modulus values for the background (matrix) and the inclusions were determined to be 20.34 kPa and 28.88 kPa, respectively.

The bottom face of the sample was fixed by gluing it on an aluminum plate using SIL-Poxy silicone adhesive. Forces were applied to the left and right faces of the composite silicone cube in the form of indentations to gently deform the cube, shown in Fig. 3(a). The terminology "indentation" throughout this paper refers to the contact pressure/traction applied on the cube via the finite circular plates attached to the force sensors. Two micrometers were utilized to measure the deformed indentations. A digital image correlation (DIC) system (DANTEC DYNAMICS, Germany) consisting of two cameras with 5 MP resolution each, an LED light source, a calibration plate, and a laptop with the "Istra 4D" software was used to measure the resulting surface displacements of the composite silicone cube (Sutton et al., 2008; Luo et al., 1993; Solav et al., 2018). In more detail, we positioned both cameras 480 mm apart from each other via a connecting rod (see Fig. 3(b) and (c)) and pointed the cameras towards the region of interest on the cube. We kept a distance of 550 mm from the center of the specimen to the center of the horizontal rail on which the cameras were mounted. The stereo-angle was 43°. Both cameras were focused well to achieve maximum image sharpness and a minimum depth of field. Using the calibration plates and a sophisticated calibration process provided by the Instra4D software, we calibrated both intrinsic and extrinsic parameters of the 2-camera system. The DIC system relies on random speckle patterns applied onto the sample's surface prior to data collection. White water-based spray-paint was used to create the random speckle pattern shown in Fig. 2(b) and (c). The displacement fields were calculated using the "Istra 4D" software, which cross-correlates camera images of the pre- and post-deformed sample.

The inverse problem was posed as a constrained optimization problem, where the boundary value problems in elasticity represent the constraints of the problem (Mei et al., 2017). In more detail, the objective function, π, given in Eq. (1) was minimized with respect to the shear modulus distribution. The objective function here was provided in discretized form using finite element shape functions, $\psi_j^e(\mathbf{x})$, for e-th element and j-th local node, where $\mathbf{x}$denotes the spatial coordinate. The shear modulus distribution was represented as unknowns on finite element mesh nodes and interpolated with linear shape functions. This methodology does not require any prior assumption about the mechanical property distribution.

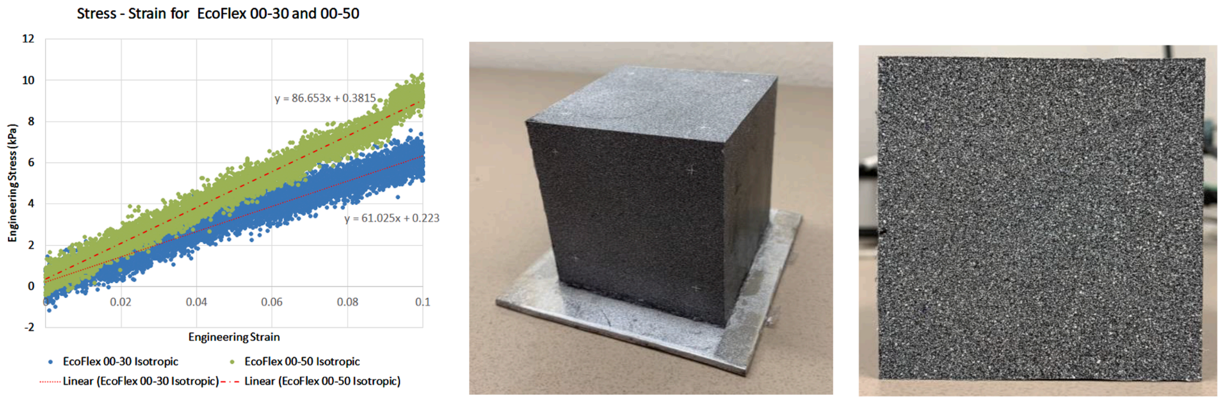

(a) (b) (c)

Fig. 2. (a) Stress versus strain curves for background material and inclusion material; (b) Speckle pattern of the cube in three-dimensional view; (c) Speckle pattern of the cube in front view.

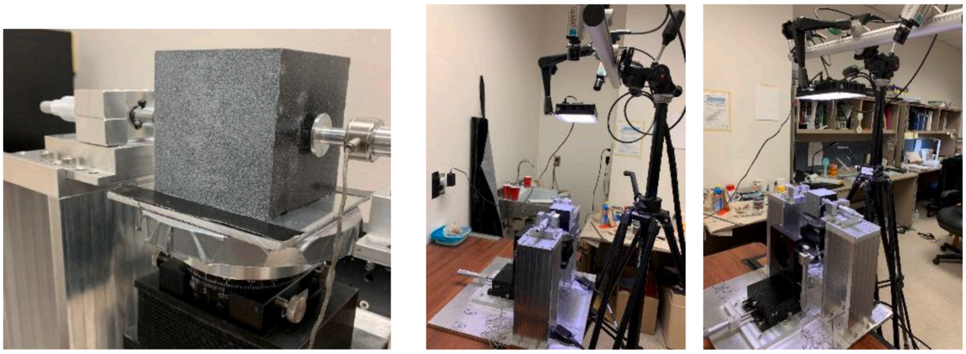

Fig. 3. (a) Experimental setup to apply force indentations to deform the cube; (b) DIC system set up to record images during sample deformation.

$$\pi = \frac{1}{2}\sum_{i=1}^{N}\left[\sum_{e=1}^{N_n}\int_{\Omega_e}\left(\sum_{j=1}^{n_e}\left(w_j^e\right)_i\psi_j^e(\mathbf{x})\left\{\left(\mathrm{u}_e^i\right)_{comp}-\left(\mathrm{u}_e^i\right)_{meas}\right\}_j\right)^2 d\Omega\right]+\frac{\alpha}{2}\sum_{e=1}^{N_n}\int_{\Omega_e}\sqrt{\sum_{j=1}^{n_e}\left|\mu_i^e\nabla\,\psi_j^e(\mathbf{x})\right|^2+c_0^2 d\Omega} \tag{1}$$

The first term in Eq. (1) depicts the displacement correlation (or matching) term and the second term depicts the regularization term. The displacement correlation term correlates computed displacements $(\mathrm{u}_e^i)_{comp}$to measured displacements $(\mathrm{u}_e^i)_{meas}$, where the computed displacements satisfy the constraint of the problem, i.e., the boundary value problems solved with the finite element methods. The regularization term penalizes oscillations in the shear modulus distribution and smoothens the final solution, where $\alpha$is the regularization factor that assigns a weight to the regularization term. Further, μ_i^edenotes the unknown nodal shear moduli and c_0 was selected to be 0.01 to avoid singularities. The total variation diminishing (TVD) regularization was utilized in this paper, since it does not penalize gradients in the shear modulus distribution (Goenezen, 2011). We solve the constrained optimization problem using the limited-BFGS method for which we evaluate the gradient of the function with respect to the nodal unknown shear moduli using the adjoint equations. To drive the inverse problem to a unique solution, the objective function accommodates N data sets obtained from utilizing varying boundary conditions on the sample. N_n is the total number of elements throughout the entire problem domain. Ω_e denotes the volume of each finite element number e and n_e is the number of local nodes on each element e. Further, $(w_j^e)_i$denotes a nodal weighting factor and was set to be 1 if nodal displacement measurement was known and 0 otherwise.

3. Results

3.1. Theoretical study for verification of MBT with synthetic displacements

We will utilize synthetic surface displacements, created by solving boundary value problems for the verification of Mechanics Based Tomography (MBT). We model the cube as an isotropic, non-homogeneous, incompressible, and linear elastic material. The mechanical properties are selected according to experimental measurements from uniaxial tensile tests. For all computations presented in this section, the constrained minimization problem was considered to be converged when the objective function (see Eq. (1)) value did not drop significantly.

The three-dimensional cube was discretized with 183,743 linear tetrahedral elements and 34,574 nodes. Each cube edge was discretized using 38 equally spaced nodes and each cube having $2 \times 37 \times 37$ triangles. Overall, the volumetric mesh was unstructured and coarse due to the computational cost of solving the inverse problem.

As shown in Fig. 4(a)–(c) the cube's bottom face was fixed and remains fixed for all subsequent models in this manuscript. Indentations were applied pair-wise, with one force applied on the left face and the other on the right face such that the force pairs are adding up to zero forces and do not cause any resultant moment. Nine pairs of indentations were applied at nine locations sequentially. Orange circles indicate areas of applied traction and the red arrows their resultant forces with their coordinates listed in Table I. To elaborate further on Table I, each force pair $i = 1, 2, 3, \ldots, 9$ consists of 2 forces, one located at $X = 0$ mm and one at $X = 70$ mm. Their Y and Z coordinates are given in Table I. Each force pair is applied separately to induce a unique surface displacement field. The origin of the coordinate system was at the bottom left corner shown in Fig. 4(d). We note that the orange circles comprised about 86 nodes, and each nodal force was set to 0.05 N, equivalent to a resultant force of about 4.3 N.

Each nodal force within the orange circles in Fig. 4 was set to 0.05 N. A total of nine pair-wise indentations were applied sequentially for each simulation (see Fig. 4(d) and Table I), resulting in 9 unique surface measurements. Furthermore, only in-plane displacement data of the front and back faces (x and z displacements) were utilized. We note that later studies in this paper will utilize out of plane displacement components as well. We also discarded displacement data sets near the edges of measured faces, since measurements along the edges are very difficult to obtain in actual experiments with a DIC system.

To mimic actual noisy measurements, we added white random Gaussian noise to the "measured" (actually synthetic) surface displacement fields of 0.1%, 1%, 5%, and 10%. We note that each noise level was applied collectively to all 3 displacement

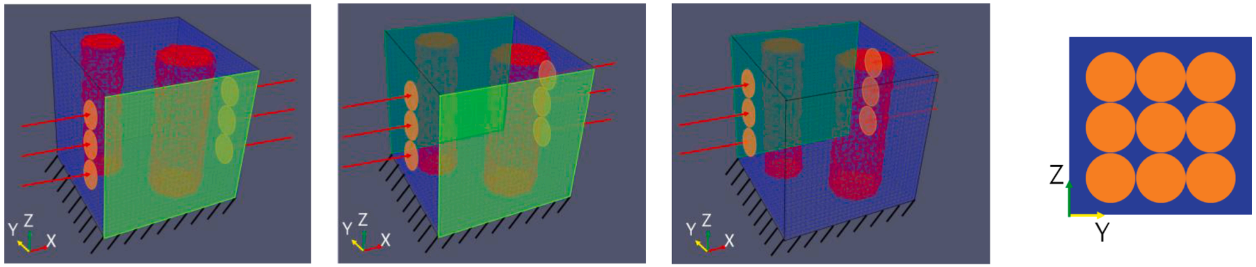

(a) (b) (c) (d)

Fig. 4. Problem domain with two stiff cylindrical inclusions surrounded by a softer background material. Orange circles indicate areas of applied traction and the red arrows their resultant forces. The green shaded faces represent the surfaces that were used to extract displacements and utilized in the tomographic inversion as the measured data. (a) Forces applied near the front face; (b) Forces applied at mid-face; (c) Forces applied near the back face; (d) Locations of all forces used with view from the right face.

Table I
Coordinates of the pair-wise resultant forces and the radius of orange circles in Fig. 4 at $X = 0$ mm and $X = 70$ mm.

Force Pair	Coordinates Y (mm)	Z (mm)	Radius (mm)
1	15.0	15.0	10.0
2	15.0	35.0	10.0
3	15.0	55.0	10.0
4	35.0	15.0	10.0
5	35.0	35.0	10.0
6	35.0	55.0	10.0
7	55.0	15.0	10.0
8	55.0	35.0	10.0
9	55.0	55.0	10.0

components. This implies that each displacement component may have slightly higher or lower noise levels than the specified one. Further, the actual noise in the measured displacement may be around 1% as discussed in Mei et al. (2017) and Gupta et al. (2014). However, this lower noise level is not guaranteed in actual experiments and will depend on several factors, such as for example the overall magnitude of the displacement, the quality of the speckle pattern, camera resolution, choice of the facet size, and grid spacing. Thus, the actual noise level could exceed 5% using a DIC system. To be on the conservative side, we have included large displacement noise levels of about 10% in this study. We also calculated the relative displacement correlation given in Eq. (2) in order to select a proper regularization factor according to Morozov's discrepancy principle (Bonesky, 2008 Dec 11).

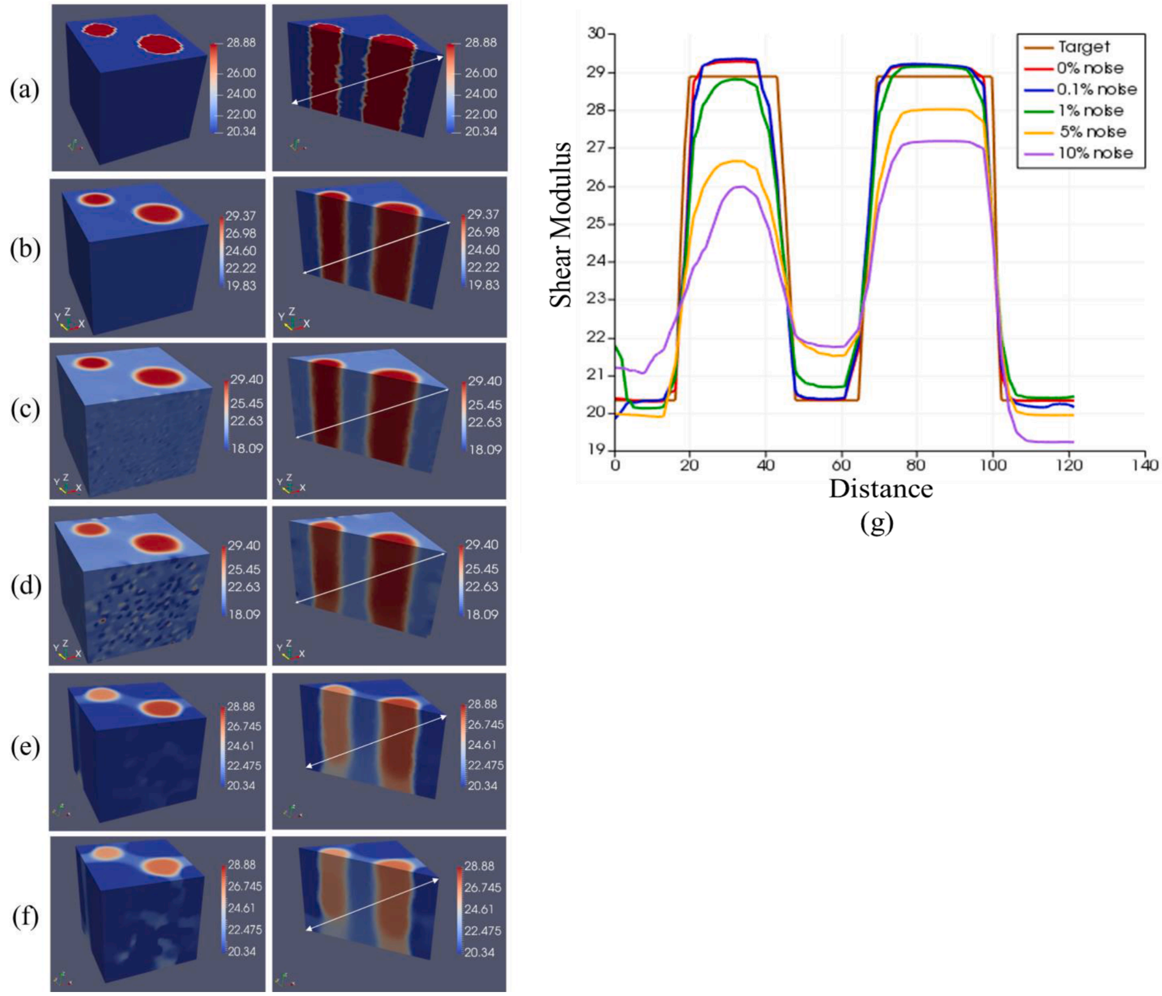

Fig. 5. (a) Target shear modulus distribution; (b) Shear modulus reconstruction with 0% noise; (c) Shear modulus reconstruction with 0.1% noise; (d) Shear modulus reconstruction with 1% noise; (e) Shear modulus reconstruction with 5% noise; (f) Shear modulus reconstruction with 10% noise (g) Comparison of reconstructed and target shear moduli along the diagonal line. Shear moduli units in [kPa] and distance in [mm].

$$\mathrm{e} = \sqrt{\frac{\sum_{i=1}^{N}\left[\sum_{e=1}^{N_n}\int_{\Omega_e}\left(\sum_{j=1}^{n_e}\left(w_j^e\right)_i\psi_j^e(\mathrm{x})\left\{\left(\mathrm{u}_e^i\right)_{comp}-\left(\mathrm{u}_e^i\right)_{meas}\right\}_j\right)^2 d\Omega\right]}{\sum_{i=1}^{N}\left[\sum_{e=1}^{N_n}\int_{\Omega_e}\left(\sum_{j=1}^{n_e}\left(w_j^e\right)_i\ \psi_j^e(\mathrm{x})\left\{\left(\mathrm{u}_e^i\right)_{meas}\right\}_j\right)^2 d\Omega\right]}} \times 100\,\% \tag{2}$$

We defined the lower and upper bound for the shear modulus value μ_i^e, in the optimization problem to be 1 kPa and 300 kPa, respectively. Fig. 5(b)–(f) show the reconstructed shear modulus distribution for 0%, 0.1%, 1%, 5%, and 10% noise, respectively, together with the target problem domain in Fig. 5(a) for comparison. The inclusions have been reconstructed well with respect to their shape and shear modulus values for all noise levels. The quality of the reconstruction slightly deteriorates with a higher noise level. Fig. 5(g) plots the shear moduli along the diagonal line shown in the clip view of Fig. 5(a)–(f). For Fig. 5(d), the color bar was rescaled. Also, for Fig. 5(e)–(f), the color bar was rescaled to the target shear modulus values. At this point, we note again that only in-plane displacement data of the front and back faces were utilized.

The computations converged after 2467, 2025, 550, 360, and 351 iterations for 0%, 0.1%, 1%, 5%, and 10% noise, respectively. It was observed that the shape and location of both, small and large inclusions were well recovered. We also observed that the values of the recovered shear moduli of the sample are close to the target value. Table II summarizes the regularization factors selected for each noise level and the relative displacement correlation. It was observed that the relative displacement correlation is about the order of the noise level for 0.1%, 1%, 5%, and 10% noise, satisfying Morozov's discrepancy principle.

In the next theoretical study, we reduced "measured" surface displacements to a minimum to test the limits of MBT utilizing the same cube model with two cylindrical stiff inclusions. To this end, we apply a pair-wise indention close to the front face and utilize the resulting displacements as the "measured" surface displacements on the front face only as depicted in Fig. 6(a). All three displacement components were assumed to be known on the green shaded face.

The resultant pair-wise forces were located at (15.0 mm, 35.0 mm) viewed from the right face. All 3 displacement components of the front face were assumed to be the measured displacement data and utilized to solve the inverse problem. However, we omitted measured displacement data of 4 layers near the edges of that face, since these are difficult to acquire experimentally. Random noise of 0.1% was added to the surface displacement field. Fig. 7(b) and (c) show the reconstructed shear modulus distributions for 0% and 0.1% noise, respectively, together with the target problem domain in Fig. 7(a) for comparison. Fig. 7(d) plots the shear moduli along the diagonal line as shown in the section view of Fig. 7(a)-(c) (second row). For Fig. 7(b)-(c) the color bar was rescaled to facilitate comparison.

The computations converged after 8678 and 8504 iterations for 0% and 0.1%, respectively. It was observed that the shape and location of the inclusion near the front were recovered, but the inclusion in the rear could not be reconstructed and appeared to be one with the homogeneous background. We also observed that the quality of the reconstructions was worse than that of using nine boundary value problems in Fig. 5, because fewer measurements were utilized for solving the inverse problem. Further, we acknowledge that the noise level of 0.1% is significantly lower than one would expect in actual displacement measurements. We have omitted results with higher noise levels, since these were significantly distorted. However, the point here was to illustrate that it is feasible to locally reconstruct inclusions if the noise level is low enough and displacements are induced locally. Table III lists the regularization factors selected for each noise level and the relative displacement correlation. It was observed that the relative displacement correlation was around the order of the noise level for 0.1% noise, satisfying Morozov's discrepancy principle.

In Fig. 8 indentation forces near the back face were applied and all displacement components x, y, and z of the cube's back face were computed. We also discarded 4 mesh layers of data near the edges of that face. The orange circles represent the regions of applied tractions and the red arrows their associated resultant forces. The coordinate of the paired resultant forces were located at (55.0 mm, 35.0 mm) viewed from the right face. Random Gaussian noise of 0.1% was added to the surface displacement field.

Fig. 9(b) and (c) represent the reconstructed shear modulus distributions for 0% and 0.1% noise, respectively, together with the target problem domain in Fig. 9(a) for comparison. Fig. 9(d) plots the shear moduli along the diagonal line shown in the clip view of Fig. 9(a)-(c). For Fig. 9(b)-(c) the color bar was rescaled.

The computations converged after 8253 and 9068 for 0% and 0.1% noise, respectively. A similar trend was observed here compared to the model from Fig. 6 and the reconstruction in Fig. 7, i.e., the inclusion near the applied force and back face was reconstructed while the one further away from those could not be detected. We observe that the reconstructed inclusion deviates somewhat from the cylindrical shape. Table IV lists the regularization factors selected for each noise level and the relative displacement correlation. It was observed that the relative displacement correlation was around the order of the noise level for 0.1% noise, according to Morozov's discrepancy principle.

In Fig. 10, we combine both data sets obtained from the models in Fig. 6 and 8.

Table II

Regularization factor, relative displacement correlation, and the number of iterations for cases presented in Fig. 5.

Noise level (%)	Regularization factor (α)	Relative displacement correlation (%)	Number of iterations
0	9.0×10^{-8}	0.0048	2467
0.1	9.0×10^{-8}	0.0659	2025
1	2.7×10^{-6}	0.6894	550
5	1.0×10^{-5}	3.9737	360
10	2.0×10^{-5}	7.9225	351

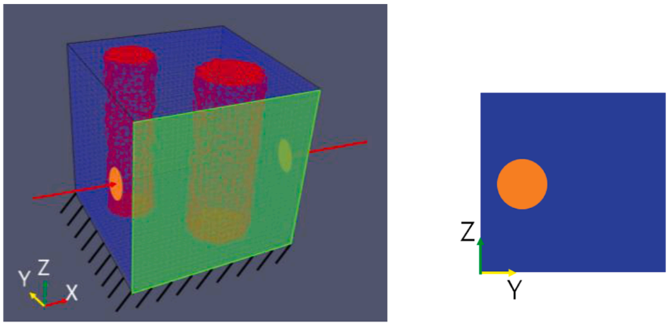

(a) (b)

Fig. 6. (a) Problem domain with two stiff cylindrical inclusions surrounded by a softer background material. Orange circles indicate areas of applied traction and the red arrows their resultant forces. The measured surface is shaded in green and the location of the pair-wise force is near the front face; (b) View from the right face.

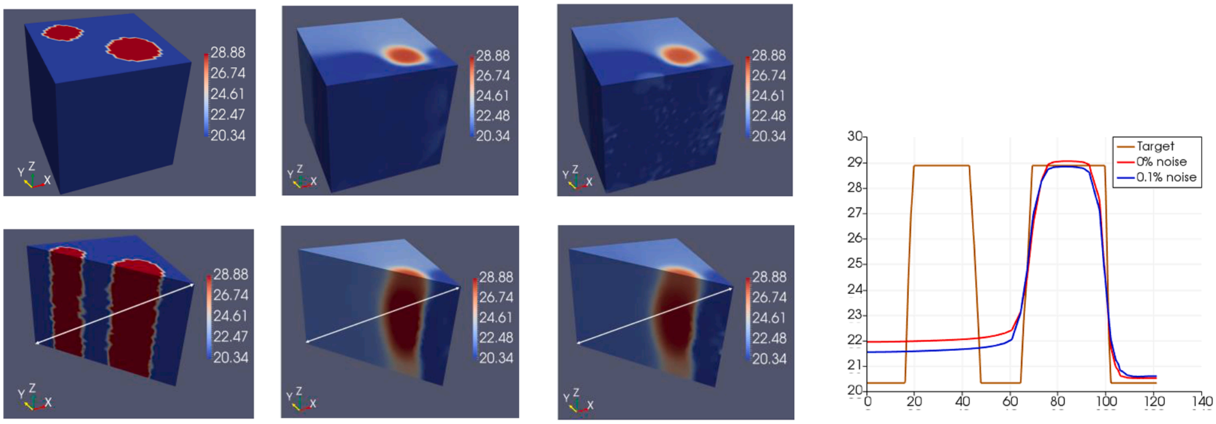

(a) (b) (c) (d)

Fig. 7. (a) Target shear modulus; (b) Shear modulus reconstruction with 0% noise, (c) Shear modulus reconstruction with 0.1% noise, (d) Comparison of reconstructed and target shear moduli along the diagonal line. Shear moduli units in [kPa] and distance in [mm].

Table III

Regularization factor, relative displacement correlation, and the number of iterations for cases presented in Fig. 7.

Noise level (%)	Regularization factor (α)	Relative displacement correlation (%)	Number of iterations
0	1.0×10^{-7}	0.0142	8678
0.1	1.0×10^{-7}	0.0676	8504

Fig. 11(b),(c) show the reconstructed shear modulus distributions for 0% and 0.1%, respectively, together with the target problem domain in Fig. 11(a) for comparison. Fig. 11(d) plots the shear moduli along the diagonal line that is shown in the section view of Fig. 11(a)–(c). For Fig. 11(b),(c) the color bar was rescaled.

The computations converged after 5620 and 4793 iterations for 0% and 0.1% noise, respectively. It was observed that the shape and location of both small and large inclusions were well recovered for both noise levels. The reconstructed shape for the inclusions deviates slightly from the cylindrical target shape for 0% and 0.1% noise. Table V lists the regularization factors selected for each noise level and the relative displacement correlation. The regularization factors were chosen such that the relative displacement correlation was about the noise level of 0.1% according to Morozov’s discrepancy principle.

Next, we increase the data set to further improve MBT. To this end, we created 5 surface displacement data sets from the application of 5 pair-wise forces on the left and right face. We extracted surface displacement fields from the front, top, and back face as the measured datasets shown in Fig. 12(a). Five more surface displacement data sets were created by applying 5 pair-wise forces on the front and back face sequentially and utilizing the corresponding surface displacement fields from the left and right face as shown in Fig. 12(b). Thus, a total of 10 surface displacement datasets were created using 10 distinct boundary conditions. For all data sets in this study, we utilized all 3 displacement components x, y, and z.

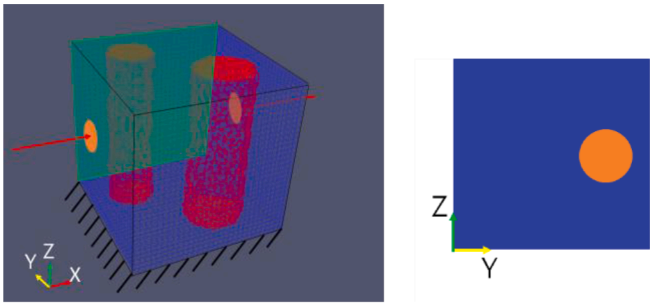

(a) (b)

Fig. 8. (a) Problem domain with two stiff cylindrical inclusions surrounded by a softer background material. Orange circles indicate areas of applied traction and red arrows their resultant forces. Pair-wise force applied near the back face. Measured surfaces are shaded in green. (b) View from the right face.

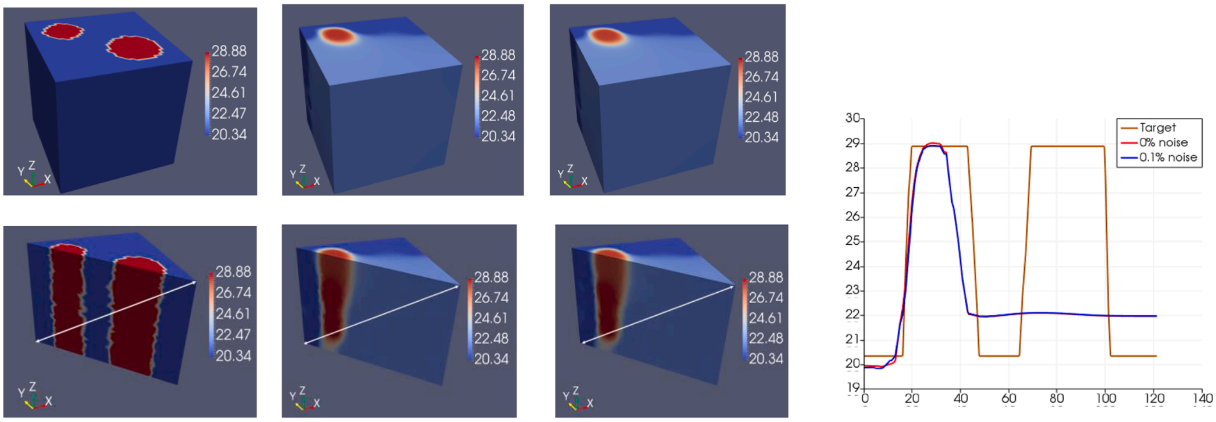

(a) (b) (c) (d)

Fig. 9. (a) Target shear modulus; (b) Shear modulus reconstruction with 0% noise; (c) Shear modulus reconstruction with 0.1% noise; (d) Comparison of reconstructed and target shear moduli along the diagonal line. Shear moduli units in [kPa] and distance in [mm].

Table IV
Regularization factor, relative displacement correlation, and the total number of iterations for the cases presented in Fig. 9.

Noise level (%)	Regularization factor (α)	Relative displacement correlation	Number of iterations
0	1.0×10^{-7}	0.0188%	8253
0.1	1.0×10^{-7}	0.0691%	9068

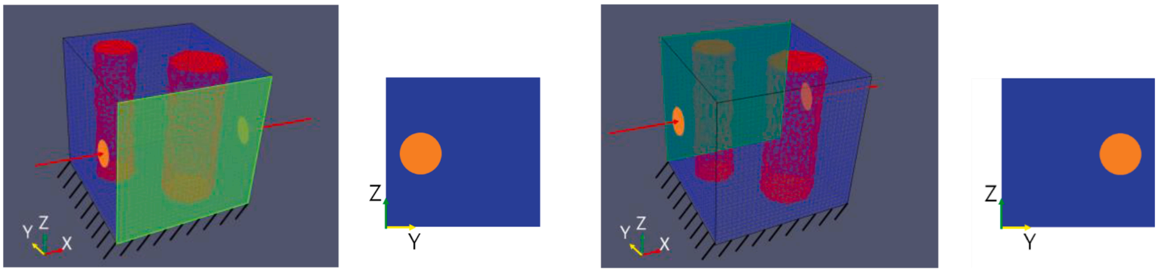

(a) (b) (c) (d)

Fig. 10. (a), (c) Problem domain with two stiff inclusions surrounded by a softer background material. Orange circles indicate areas of applied traction and red arrows their resultant forces. Measured surfaces are shaded in green. (b), (d) View from the right face.

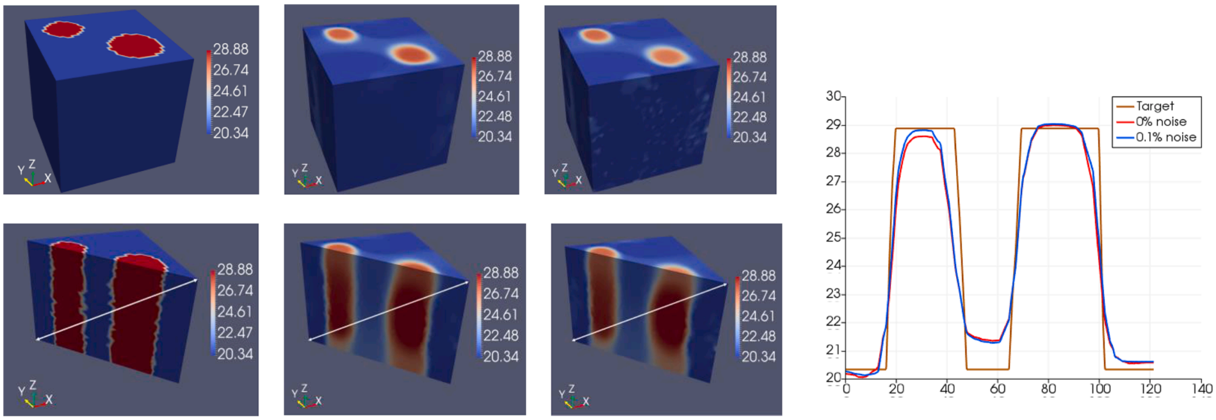

(a) (b) (c) (d)

Fig. 11. (a) Target shear modulus, (b) Shear modulus reconstruction with 0% noise, (c) Shear modulus reconstruction with 0.1% noise, (d) Comparison of reconstructed and target shear moduli along the diagonal line. Shear moduli units in [kPa] and distance in [mm].

Table V
Regularization factor, relative displacement correlation, and the number of iterations for cases presented in Fig. 11.

Noise level (%)	Regularization factor (α)	Relative displacement correlation (%)	Number of iterations
0	1.0×10^{-7}	0.0123	5620
0.1	1.0×10^{-7}	0.0678	4793

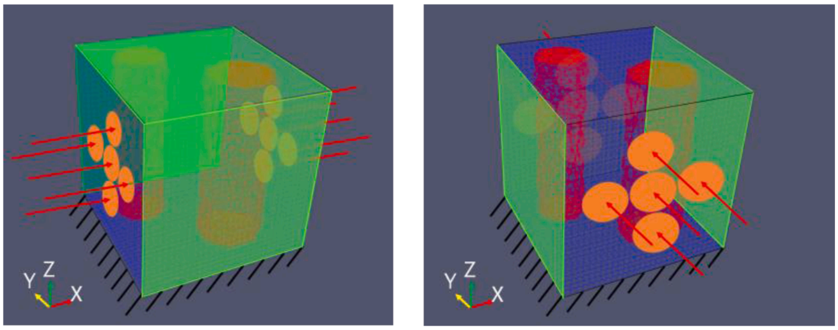

(a) (b)

Fig. 12. Problem domain with two stiff cylindrical inclusions surrounded by a softer background material. Orange circles indicate areas of applied traction and red arrows their resultant forces. Measured surfaces are shaded in green. (a) Measuring front, back, and top faces; (b) Measuring left and right faces.

The coordinates of the resultant forces are listed in Table VI. The number of nodal forces for each indentation on the surfaces are reported in the table as well. Each nodal force was set to 50 mN.

Random Gaussian noise of 0.1%, 1%, 5%, and 10% was added to all displacement components to mimic noisy measurements. Fig. 13(b)–(f) show the reconstructed shear modulus distributions for 0%, 0.1%, 1%, 5%, and 10% noise, respectively, together with

Table VI
Coordinates of the pair-wise forces.

Force coordinates on left and right face		Force coordinates on front and back face			
Y (mm)	Z (mm)	X (mm)	Z (mm)	Radius (mm)	Number of nodal forces
16.86	34.41	16.86	34.41	10.0	91
35.60	15.67	35.60	15.67	10.0	86
35.60	34.41	35.60	34.41	10.0	90
35.60	53.14	35.60	53.14	10.0	91
54.33	34.41	54.33	34.41	10.0	86

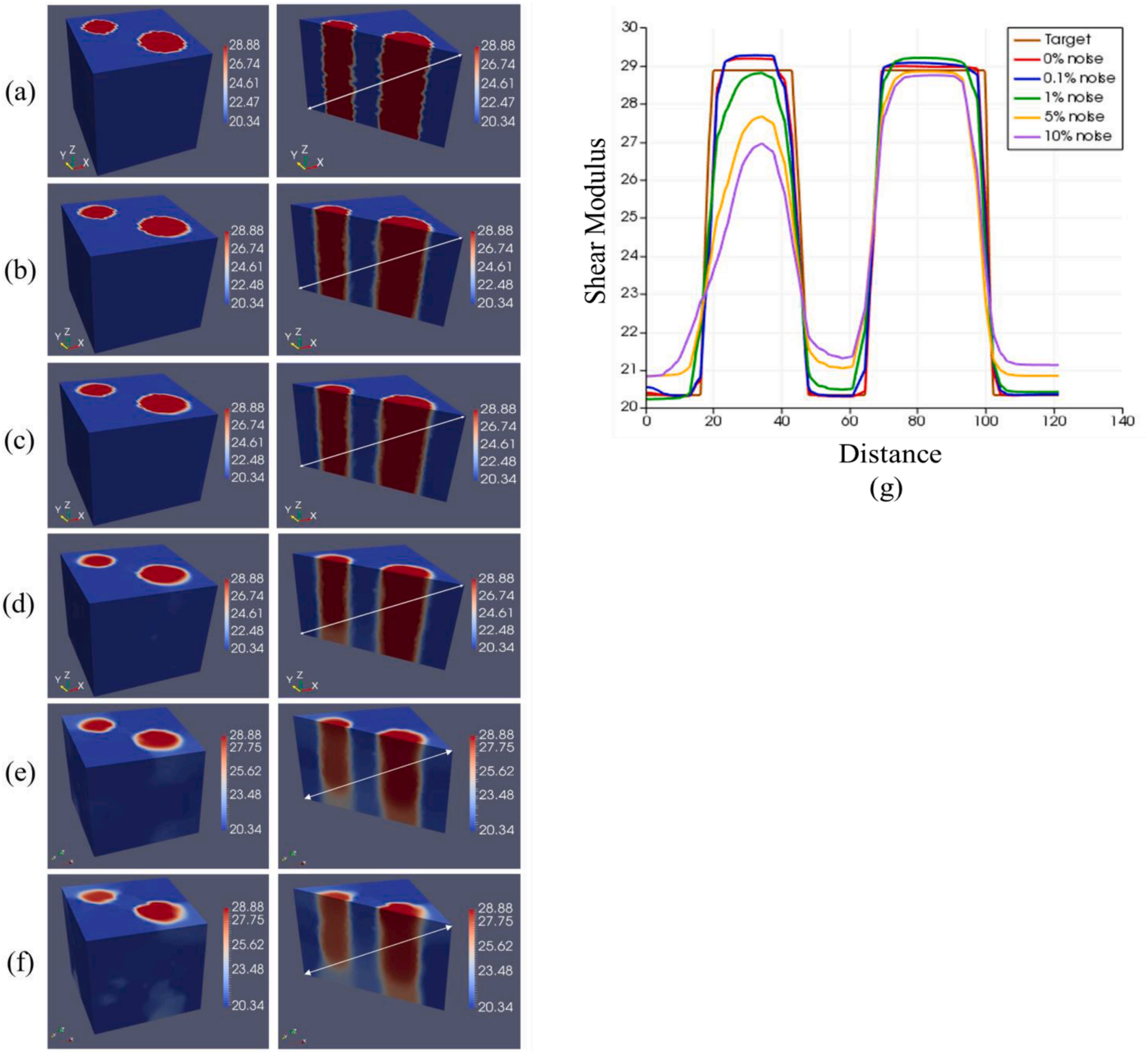

Fig. 13. (a) Target shear modulus; (b) Shear modulus reconstruction with 0% noise; (c) Shear modulus reconstruction with 0.1% noise; (d) Shear modulus reconstruction with 1% noise; (e) Shear modulus reconstruction with 5% noise; (f) Shear modulus reconstruction with 10% noise (g) Comparison of reconstructed and target shear moduli along the diagonal line. Shear moduli units in [kPa] and distance in [mm].

the target problem domain in Fig. 13(a) for comparison. Fig. 13(g) plots the shear moduli along the diagonal line as shown in the section view of Fig. 13(a)–(f).

The computations converged after 2780, 1317, 391, 318, and 296 iterations for 0%, 0.1%, 1%, 5%, and 10% noise, respectively. We observe that both, small and big inclusions were very well reconstructed with respect to their shapes and shear modulus values for all noise levels. In Table VII the regularization factors and the relative displacement correlation are reported. It is observed that the

Table VII
Regularization factor, relative displacement correlation, and the number of iterations for the reconstructions presented in Fig. 13.

Noise level (%)	Regularization factor (α)	Relative displacement correlation (%)	Number of iterations
0	1.0×10^{-7}	0.0059	2780
0.1	5.0×10^{-7}	0.0780	1317
1	1.0×10^{-5}	0.7791	391
5	7.0×10^{-6}	3.9022	318
10	1.0×10^{-5}	7.7485	296

relative displacement correlation is in the order of the noise level for 0.1%, 1%, 5%, and 10% noise.

Next, we investigate the effect of uncertainties in the locations of applied indentation on MBT. To this end, we deviate the resulting force locations by 0.45 mm, 0.90 mm, and 1.80 mm. These quantities were chosen based on our experience with conducting the experiments. Here it may be suitable to non-dimensionalize the uncertainties in applied force location with the indenter radius that translates to 4.5%, 9%, and 18% deviation of the resulting force. We will use the surface displacement data sets created from the model in Fig. 12 and deviate the force location when solving the inverse problem.

First, we deviated the location of the resultant forces by about 0.45 mm (4.5%) in the diagonal direction. The deviated force locations are listed in Table VIII together with the total number of nodal forces for each indentation.

Fig. 14(b)-(d) show the reconstructed shear modulus distribution for 0%, 0.1%, and 1% noise, respectively, together with the target shear modulus distribution in Fig. 14(a) for comparison. For Fig. 14(b)-(d) the color bar was rescaled. Fig. 14(e) provides a plot of the shear modulus values along the diagonal lines in Fig. 14(a)–(d).

The computations converged after 355, 353, and 351 iterations for 0%, 0.1%, and 1% noise, respectively. We observe that the shape of both, small and large inclusions deteriorated significantly from a cylindrical inclusion. In Table IX, we list the regularization factors selected for each noise level and the relative displacement correlation.

Next, we deviated the location of the resultant forces by about 0.9 mm (9%) in the diagonal direction. The deviated force locations are listed in Table X together with the total number of nodal forces for each indentation.

Fig. 15(b)–(d) shows the reconstructed shear modulus distribution for 0%, 0.1%, and 1% noise, respectively, together with the target problem domain in Fig. 15(a) for comparison. For Fig. 15(b)–(d) the color bar was rescaled. Fig. 15(e) provides a plot of the shear modulus values along the diagonal lines in Fig. 15(a)-(d).

The computations converged after 724, 626, and 827 iterations for 0%, 0.1%, and 1% noise, respectively. We observe that the shape of both, small and large inclusions deteriorated significantly from a cylindrical inclusion. In Table XI, we list the regularization factors selected for each noise level and the relative displacement correlation.

Next, we deviated the location of the resultant forces by about 1.8 mm (18%) in the diagonal direction. The deviated force locations are listed in Table XII together with the total number of nodal forces for each indentation.

The computations converged after 1666, 2011, and 1547 iterations for 0%, 0.1%, and 1% noise, respectively. We observe that the overall shear modulus reconstruction is significantly off from the target shear modulus distribution. In Table XIII, we list the regularization factors selected for each noise level and the relative displacement correlation.

A comparison of the shear modulus reconstructions between Fig. 13 (without any deviation of force locations) and Figs. 14-16 (with deviations in force locations) reveals that the deteriorations in the reconstructions are dramatically amplified when the force locations were slightly deviated.

3.2. Validation of MBT with experimental data

In this section we *validate* Mechanics Based Tomography (MBT) with experimental data using a DIC system on the composite silicone cube described in the Method's section. About 2 mm indentations were applied on the cube's surface shown in Fig. 17(a). In the Instra-4D software, we specified a grid spacing of 33 pixels yielding a total of about 1365 (varies for each face) grid points and a facet (subset) size of 43 pixels. Each facet consists of a minimum of 9 speckles. The average speckle size was about 5 pixels and ranged from 3 to 12 pixels. The actual speckle size in physical dimensions varied from 260 μm to 330 μm. Fig. 17(a) illustrates a grid on the cube's face using the Instra4D software.

The Instra4D software computes the measured displacements on the grid points. However, the grid points from the Instra software are not aligned with the nodes from the finite element mesh for the inverse computations. Thus, we linearly interpolated displacement measurements from the Instra grid points onto the finite element mesh nodes. Furthermore, each measurement was processed via the Instra software with respect to a local coordinate system depicted in Fig. 17(b). We transformed these local coordinates onto a global coordinate system (see Fig. 17(c)) via the standard transformation:

$$\boldsymbol{X}_{Global} = \boldsymbol{R}\,\boldsymbol{X}_{local} + \boldsymbol{T} \tag{3}$$

for each measurement. In this equation, **R, T,** $\boldsymbol{X}_{Global}$, and $\boldsymbol{X}_{local}$ denote the rotation matrix, translation vector, global coordinates, and local coordinates. Further, we inspected measured displacement components and sometimes discarded those that appeared to be noise dominated. For example, only in-plane displacement components (X and Z) were utilized from the measurements of the front face for two of the pair-wise indentations closer to the top face shown in Fig. 18(a). Also, only in-plane displacement components were used

Table VIII
Coordinates of the 10 pair-wise resultant forces after 0.45 mm (4.5%) deviation.

Force coordinates on left and right face		Force coordinates on the front and back face			
Y (mm)	Z (mm)	X (mm)	Z (mm)	Radius (mm)	The number of nodal forces
17.18	34.70	17.18	34.70	10.0	88
35.30	15.85	35.30	15.85	10.0	86
35.30	34.70	35.30	34.70	10.0	86
35.30	53.52	35.30	53.52	10.0	86
53.76	34.70	53.76	34.70	10.0	86

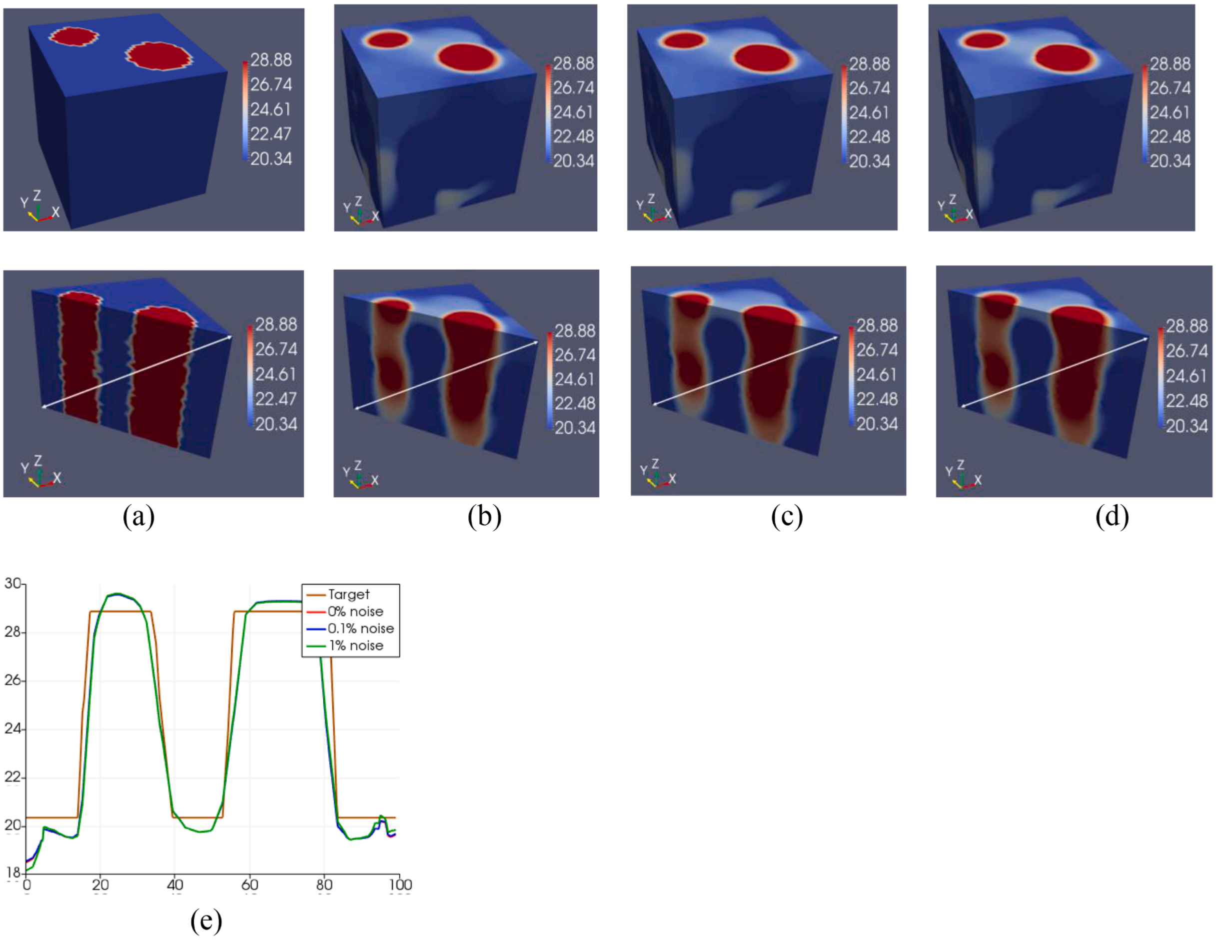

Fig. 14. (a) Target shear modulus; (b) Shear modulus reconstruction with 0% noise; (c) Shear modulus reconstruction with 0.1% noise; (d) Shear modulus reconstruction with 1% noise; (e) Comparison of reconstructed and target shear moduli along the line. Shear moduli units in [kPa] and distance in [mm].

Table IX

Regularization factor, relative displacement correlation, and the number of iterations for the reconstructions presented in Fig. 14.

Noise level (%)	Regularization factor (α)	Relative displacement correlation (%)	Number of iterations
0	5.0×10^{-5}	1.8429	355
0.1	5.0×10^{-5}	1.8439	353
1	5.0×10^{-5}	1.9938	351

Table X

Coordinates of the 10 pair-wise resultant forces after 0.9 mm (9%) deviation.

Force coordinates on left and right face		Force coordinates on front and back face			
Y (mm)	Z (mm)	X (mm)	Z (mm)	Radius (mm)	Number of nodal forces
17.50	35.00	17.50	35.00	10.0	88
35.00	16.10	35.00	16.10	10.0	88
35.00	35.00	35.00	35.00	10.0	88
35.00	53.90	35.00	53.90	10.0	88
53.20	35.00	53.20	35.00	10.0	86

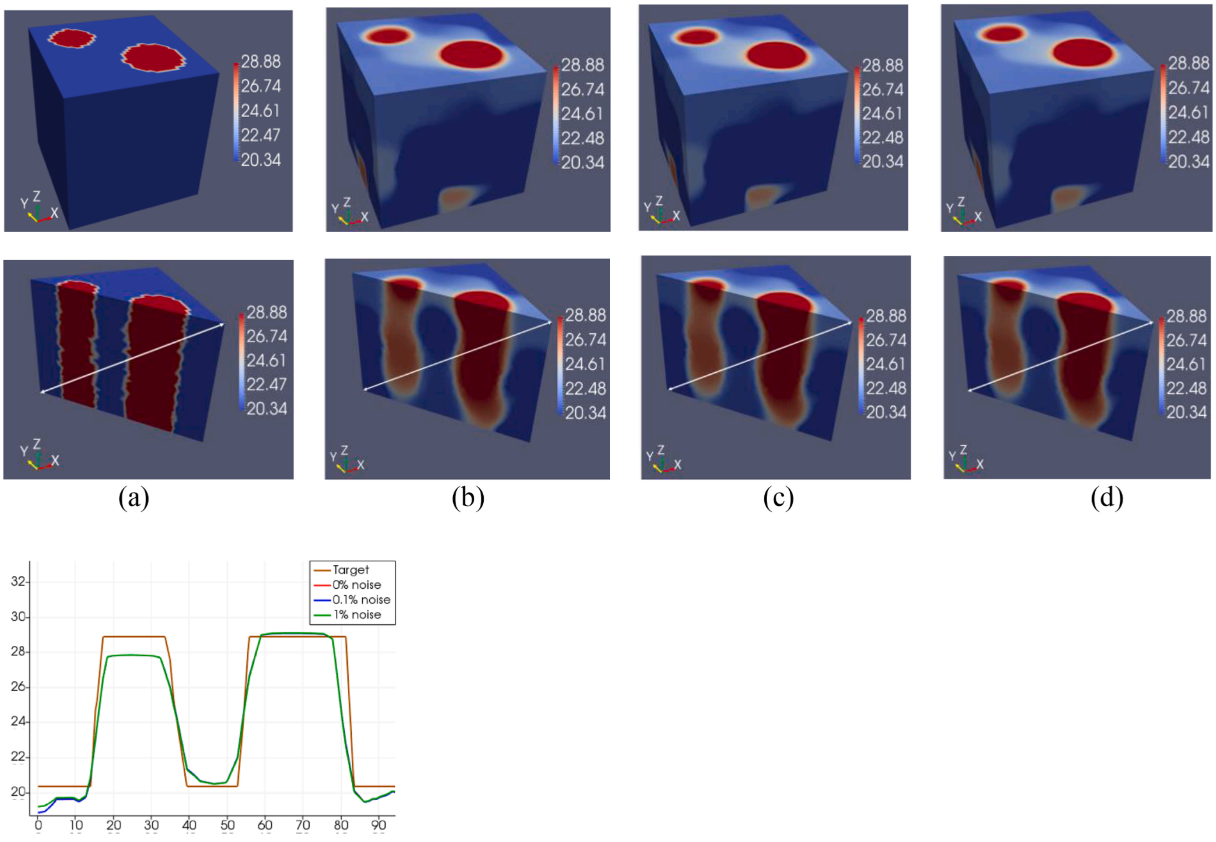

(e)

Fig. 15. (a) Target shear modulus; (b) Shear modulus reconstruction with 0% noise; (c) Shear modulus reconstruction with 0.1% noise; (d) Shear modulus reconstruction with 1% noise; (e) Comparison of reconstructed and target shear moduli along the line. Shear moduli units in [kPa] and distance in [mm].

Table XI
Regularization factor, relative displacement correlation, and the number of iterations for cases presented in Fig. 15.

Noise level (%)	Regularization factor (α)	Relative displacement correlation (%)	Number of iterations
0	1.0×10^{-4}	2.4778	724
0.1	1.0×10^{-4}	2.4785	626
1	1.0×10^{-4}	2.5949	827

Table XII
Coordinates of the 10 pair-wise resultant forces after 1.8 mm (18%) deviation.

Force coordinates on left and right face		Force coordinates on front and back face			
Y (mm)	Z (mm)	X (mm)	Z (mm)	Radius (mm)	Number of nodal forces
18.14	35.60	18.14	35.60	10.0	87
34.41	16.53	34.41	16.53	10.0	87
34.41	35.60	34.41	35.60	10.0	90
34.41	54.66	34.41	54.66	10.0	91
52.07	35.60	52.07	35.60	10.0	86

from the measurements of the back face for two pair-wise indentations closer to the top face shown in Fig. 18(b). Finally, the displacement component aligned with the direction of the indentation force and the out-of-plane displacement component were utilized from the measurement of the top face shown in Fig. 18(d). For all other measurements we used all three displacement components for the inverse computations. We discarded five layers of displacement measurements starting from the bottom edge of the front and back face in the inverse computations. Additionally, three layers of displacement measurements were discarded on those

Table XIII
Regularization factor, relative displacement correlation, and the number of iterations for cases presented in Fig. 16.

Noise level (%)	Regularization factor (α)	Relative displacement correlation (%)	Number of iterations
0	2.0×10^{-4}	4.3797	1666
0.1	2.0×10^{-4}	4.3827	2011
1	2.0×10^{-4}	4.4530	1547

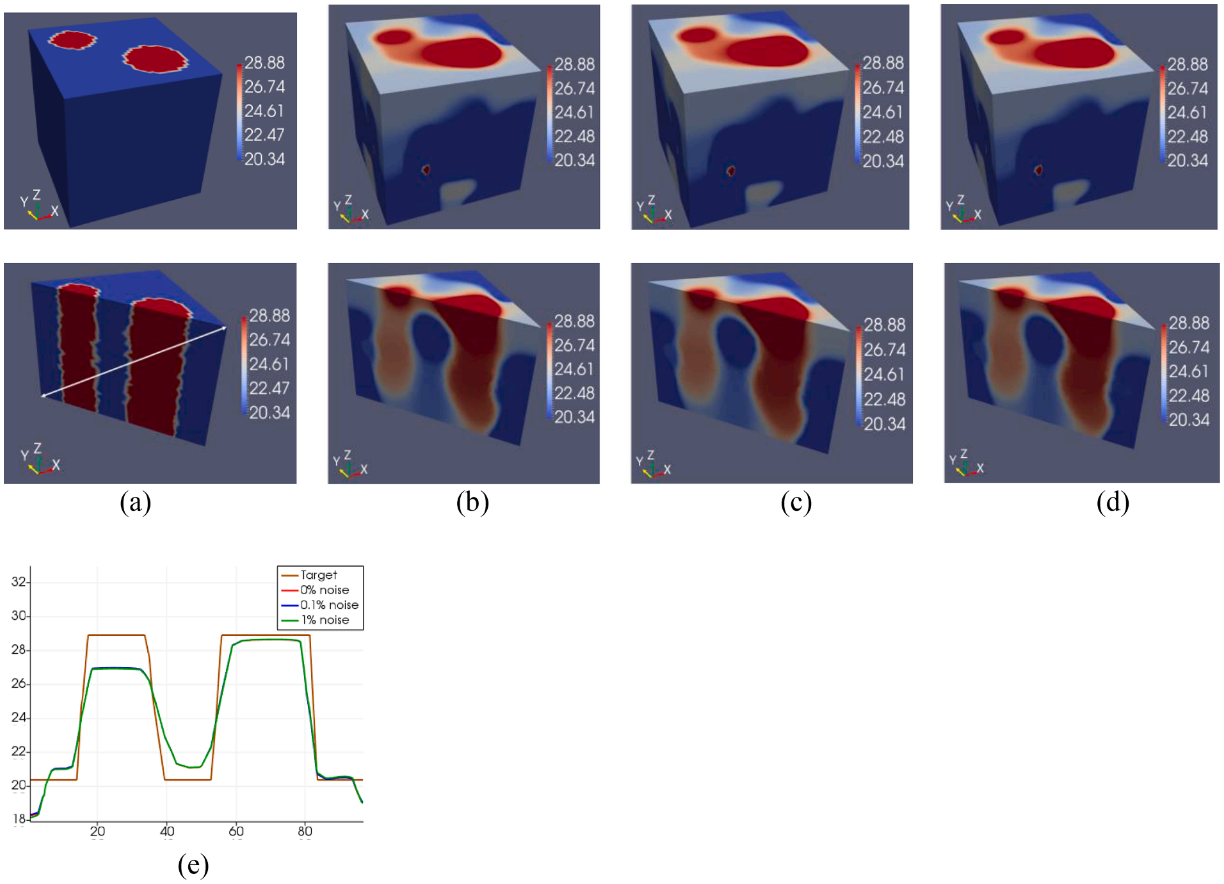

(a) (b) (c) (d)

(e)

Fig. 16. (a) Target shear modulus; (b) Shear modulus reconstruction with 0% noise; (c) Shear modulus reconstruction with 0.1% noise; (d) Shear modulus reconstruction with 1% noise; (e) Comparison of reconstructed and target shear moduli along the line. Shear moduli units in [kPa] and distance in [mm].

same faces starting from the top edges. All nine pairs of indentations were applied at nine different locations sequentially. The finite element mesh has a total of 34,574 nodes, and equals the total number of unknown shear moduli to be solved for. The coordinates of the resultant forces on the left and the right sides are listed in Table I. Since no force measurements were utilized to solve the inverse problem and only displacement boundary conditions were prescribed, the shear modulus distribution could be reconstructed only up to a constant multiplicative factor (Mei et al., 2017).

Fig. 19 compares the displacement and strain fields from a simulation (top row) and from an experiment (bottom row). We observe that the displacement and strain fields closely match. We conclude that the measured displacement fields are suitable to be used in the inverse computations.

Fig. 20(b) shows the relative shear modulus reconstructions, i.e., shear modulus distribution determined up to a multiplicative factor, in different views. The target shear modulus distribution in Fig. 20(a) is also provided for comparison. It was observed that both small and large inclusions have been well reconstructed with respect to their shapes except near the bottom edge since five layers of displacement data were discarded in that region. Fig 20(c) provides the relative shear modulus plot along the diagonal line of the section cuts. While the shear modulus value of the smaller inclusion has been well recovered, the larger inclusion overestimates the shear modulus value significantly. The regularization factor, the relative displacement correlation, and the number of iterations associated with the computation in Fig. 20(b) were selected to be 9.0×10^{-5}, 2.46%, and 3000, respectively. Overall, this final

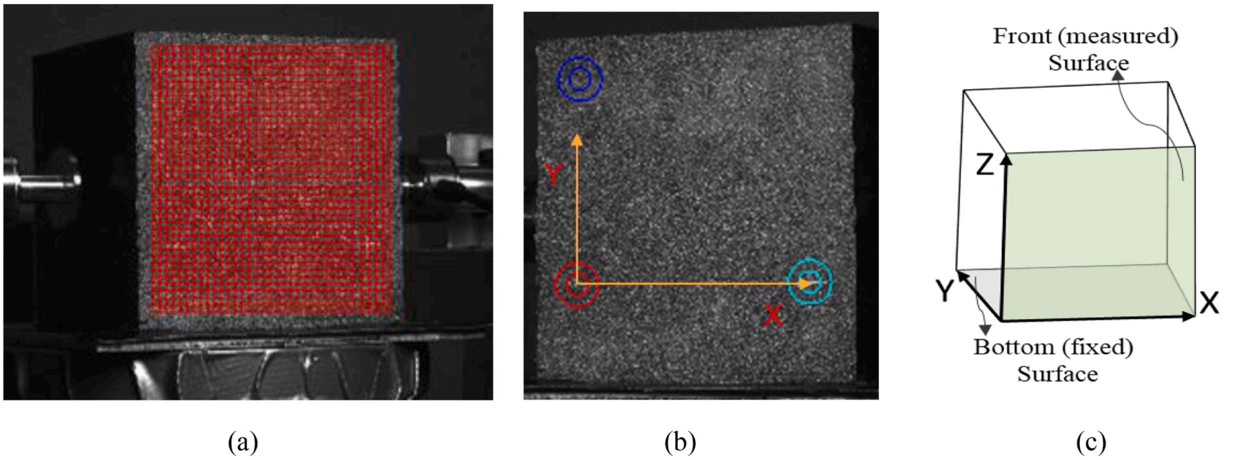

Fig. 17. (a) Grid from DIC software Instra4D with grid-spacing of 33 pixels; (b) Local coordinate system associated with one measurement; (c) Global coordinate system.

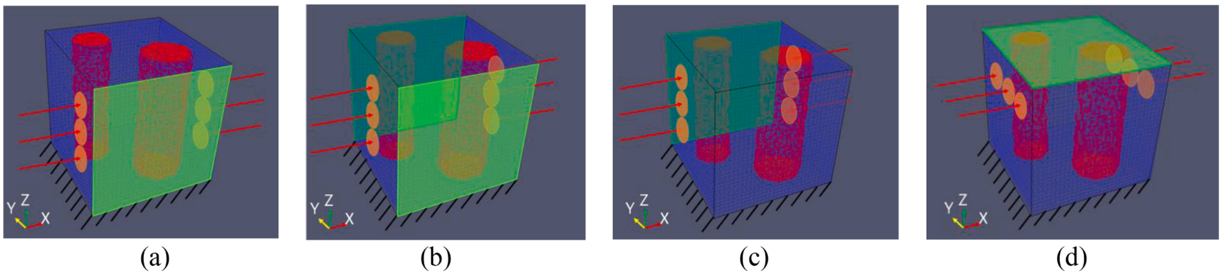

Fig. 18. Problem domain with two stiff cylindrical inclusions surrounded by a softer background material. Orange circles indicate areas of applied traction and red arrows their resultant forces. Measured surfaces are shaded in green. (a) Measuring front face; (b) Measuring front and back faces; (c) Measuring back face; (c) Measuring top face.

reconstruction with experimental data sets demonstrates that MBT has potential as a novel tomographic imaging technology.

4. Discussion

In this paper, we presented the *verification* and *validation* of a newly developed solid mechanics based tomography methodology to map the shear modulus distribution of a composite sample from limited surface displacement measurements. We termed this technology as Mechanics Based Tomography (MBT). This technology differs from other works in that we did not make any major assumption about the shear modulus distribution. We solely provide a reasonable yet wide range for the minimum and maximum value of the shear modulus in the search region of the optimization method.

For the *verification* of MBT, we conducted a theoretical study utilizing synthetic displacement data sets that were obtained from solving boundary value problems using finite element methods. The problem domain was modeled to be a composite cube with two cylindrical inclusions. Before utilizing these data sets in the inverse computations, we augmented them with random Gaussian noise to mimic noisy displacement measurements. We observed that the target shear modulus distribution was well recovered and the cylindrical inclusions were clearly visualized. The reconstructions deteriorated slightly with increasing noise levels. Furthermore, we have shown that the shear modulus reconstructions improved as the data sets were enriched, i.e., by increasing the number of surface displacement measurements using distinct boundary conditions. We have also analyzed the effects of uncertainties in the indenter location and concluded that these dramatically change the quality of the reconstructions and dominate the effect of noise in displacement measurements. Other uncertainties that have not been investigated in this paper include the geometrical representation of the sample, where a perfect cube was assumed in the MBT.

In Figs. 6 and 7, we analyzed the feasibility to map the shear modulus distribution using one synthetic measurement of one face only. We chose the front face and applied one pair wise indentation near that face only. The reconstructions surprisingly represented the front cylindrical inclusion quite well, while the inclusion on the opposite side was not detected at all. Similarly, in Figs. 8 and 9, we utilized the measurements of the back face and applied one pair wise indentation near that face only. This recovered the cylindrical inclusion near the back face, while the cylindrical inclusion near the front face remained undetected. The reason for these observations is that the inclusions further away from the measured surface do not affect the surface displacement field much. Thus, the feasible

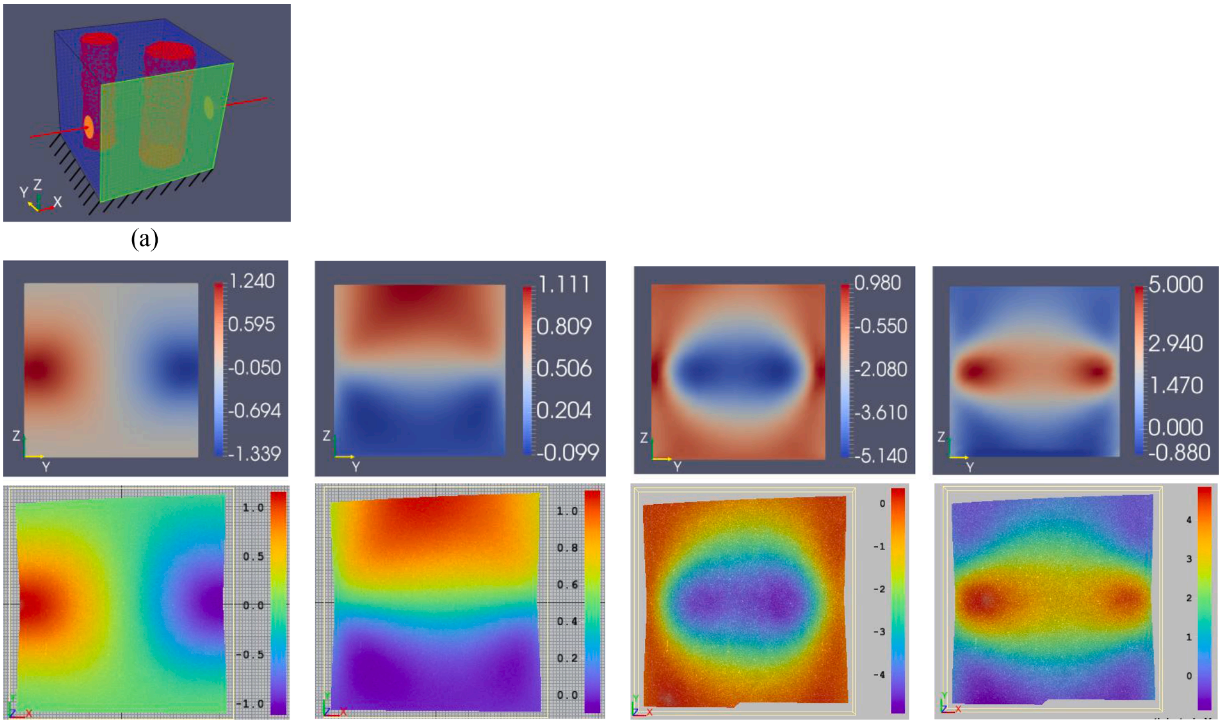
(a)

(b) (c) (d) (e)

Fig. 19. (a) Location of indentation and measured surface. (b) X-displacement field component from simulation (top) and experiment (bottom). (c) Z-displacement field component from simulation (top) and experiment (bottom). (d) X-normal strain field component from simulation (top) and experiment (bottom), (e) Z-normal strain field component from simulation (top) and experiment (bottom). Displacement units are in [mm].

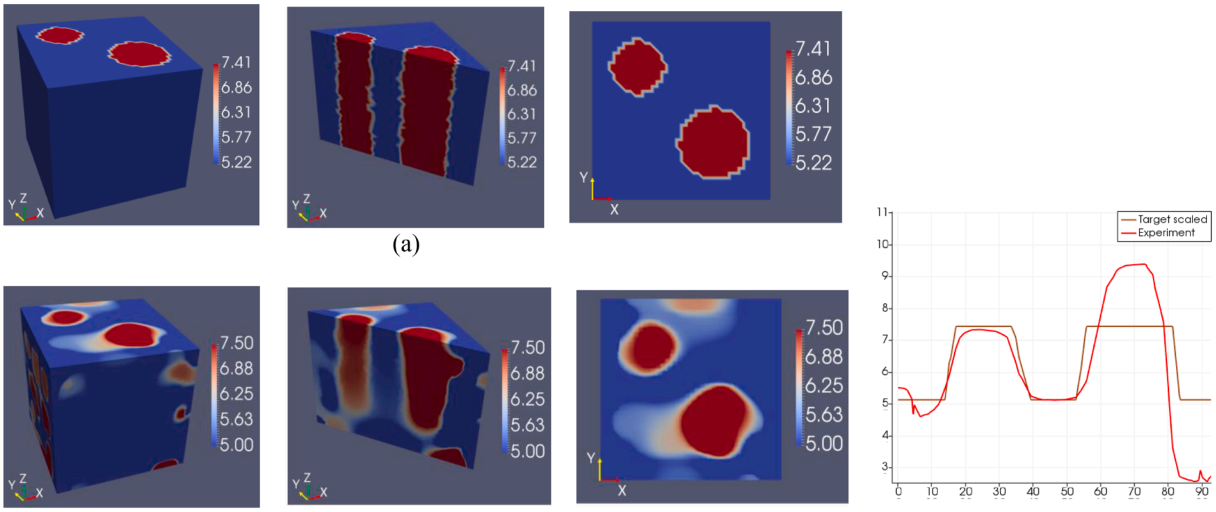
(a)

(b) (c)

Fig. 20. (a) Target shear modulus; (b) Shear modulus reconstruction with DIC displacement data; (c) Comparison of reconstructed and target shear moduli. Shear moduli units are non-dimensional and the distance is in [mm].

solutions for the shear modulus distributions distant from the measurement is infinite. However, the objective function contains a regularization term which becomes smallest when the shear modulus distribution is homogeneous. Thus, from these infinitely many solutions, the inverse problem solution converges to the locally homogeneous one. We conclude that this technology is capable of recovering local reconstructions within a large specimen by inducing and measuring displacements near the region of interest.

In the theoretical study, we have shown that it is feasible to reconstruct the 3D shear modulus distribution of the composite cube using synthetic displacement measurements in 2D only. This is an important conclusion since this does not seem to be obvious. Further it may be of interest for other researchers in future work to use only one camera and 2D DIC for 3D reconstructions, due to the cost of special cameras such as high resolution or high-speed cameras. We emphasize however, that no high speed camera or high resolution camera was required nor utilized in this work.

The *validation* of MBT was followed with experimental displacement measurements on a similar cube that we fabricated using silicone material. The reconstructions were promising, yet not as accurate as in the theoretical study. One reason for this may be due to a high noise level in the displacement measurements. Further, the noise type that may not be represented exactly as random Gaussian noise as was done in the verification part of this work. Additional uncertainties leading to deteriorated results could be due to misalignment of pair-wise forces leading to a bending and twisting mode of the specimen. Furthermore, the fixed bottom face in the finite element model does not represent the exact support in our experiments, since the cube glued to the bottom slightly detaches near the edges. Also, the composite sample was modeled to be a perfect cube, while the actual fabricated cube had deviations of about one millimeter along the edge lengths.

Future work will involve additional experiments on samples with different geometries and shear modulus distributions to demonstrate the robustness of this method. Furthermore, future work will also involve studies to detect the mechanical property distribution of other constitutive equations to model anisotropic, nonlinear, and viscoelastic materials. We anticipate that it will be harder to recover these mechanical property distributions than the linear elastic property distribution utilized in this paper. This may require that (1) the noise in the measured surface displacement field is reduced significantly, (2) force locations are precisely known and modeled accurately, (3) the region of interest to be imaged is not too distant from the measured surfaces as was demonstrated in this paper in Figs. 6–9, and (4) a rich set of distinct surface displacement fields from various applied boundary conditions is added in addition to the indentations presented in this paper, e.g. shear forces. These points could be facilitated using automated systems with robotics and high-resolution cameras.

This work presents the first verification and validation of MBT. We acknowledge that this work is still at its infancy, and more effort is needed to tailor this method to specific applications in various fields. It could potentially be employed as a novel screening or diagnostic tool in early breast tumor detection. It could also aid in the maintenance of vital civil engineering infrastructure, provide quality assurance of engineered materials, or monitor engineered tissues for their biomechanical consistency.

5. Conclusion

We have demonstrated feasibility of Mechanics Based Tomography (MBT) on a cubic composite solid to visualize the interior composition of the sample based on changes of the shear modulus, here in particular, to identify and visualize two cylindrical inclusions with differing diameters. This technology relies on measured surface displacement fields using a digital image correlation system with digital cameras. Thus, the experimental tools required for MBT are relatively cheap.

MBT could be used to screen for breast tumors in addition to currently existing methods such as ultrasound, mammography, or magnetic resonance imaging (MRI) in order to increase the sensitivity and specificity of the outcome. It could potentially also aid in various fields in engineering to analyze the interior structure and integrity of engineering materials. Future work needs to include application to particular disciplines and investigation of data requirements for unique and accurate reconstructions. Furthermore, modeling efforts need to be improved and were conducted with highly primitive tools to provide a proof of concept in this paper.

Declaration of Competing Interest

The authors declare that they have no known competing financial interests or personal relationships that could have appeared to influence the work reported in this paper.

Author Contributions

Dr. Sevan Gonezen: Advising students on this project; developing methods and algorithms; writing paper.

Baik Jin Kim: Processing data and running simulations, writing paper, conducting experiments.

Maulik Kotecha: Designing experiment protocols, conducting experiments, post-processing experiment data, contributing to paper write up.

Ping Luo: Parallelizing inverse program with MPI.

Dr. Mohammad R. Hematiyan: Developing methods; contributing to paper write up.

Acknowledgments

The authors would like to acknowledge partial funding of this project from the National Science Foundation under Grant No. CMMI #1663435 and thank for their support. The authors would also like to thank the High Performance Research Computing at Texas A&M University for their computing resources, and Dr. Arun Srinivasa's group and Dr. Terry Creasy for providing access to their Instron tensile testing machine and help to use it for the homogeneous samples.

References

Vicente, M.A., Minguez, J., Gonzalez, D.C., 2017. In: Halefoglu, A.M. (Ed.). IntechOpen, Rijeka.

Yu, B., Bradley, R.S., Soutis, C., Withers, P.J., 2016. A comparison of different approaches for imaging cracks in composites by X-ray microtomography. Philos. Trans. A Math. Phys. Eng. Sci. 374 (2071), 20160037.

Wiskin, J.W., Borup, D.T., Iuanow, E., Klock, J., Lenox, M.W., 2017. 3-D nonlinear acoustic inverse scattering: algorithm and quantitative results. IEEE Trans. Ultrason. Ferroelectr. Freq. Control 64 (8), 1161–1174.

Fan, C., Zhang, L., Jia, W., Yang, L., Sun, F., 2017. Inverse identification of effective thermal conductivity based on surface temperature measurement: an analysis of effecting factors. Heat Transf. Res. 48 (10), 915–933.

Hematiyan, M.R., Khosravifard, A., Shiah, Y.C., 2015. A novel inverse method for identification of 3D thermal conductivity coefficients of anisotropic media by the boundary element analysis. Int. J. Heat. Mass Transf. 89, 685–693.

Santosa, F., Vogelius, M., 1991. A computational algorithm to determine cracks from electrostatic boundary measurements. Int. J. Eng. Sci. 29 (8), 917–937.

Tanaka, M., Yamagiwa, K., 1989. A boundary element method for some inverse problems in elastodynamics. Appl. Math. Model. 13 (5), 307–312.

Roecker, S., McLaughlin, J., Baker, B., 2010. A finite-difference algorithm for full waveform teleseismic tomography. Int. J. Geophys. 181, 1017–1040.

Zheglova, P., McLaughlin, J.R., Roecker, S.W., Yoon, J.R., Renzi, D., 2012. Imaging quasi-vertical geological faults with earthquake data. Geophys. J. Int. 189 (3), 1584–1596.

Schnur, D.S., Zabaras, N., 1992. An inverse method for determining elastic material properties and material interface. Int. J. Numer. Methods Eng. 33 (10), 2039–2057.

Hajhashemkhani, M., Hematiyan, M.R., Goenezen, S., 2018. Identification of material parameters of a hyper-elastic body with unknown boundary conditions. J. Appl. Mech. 85 (5).

Van Houten, E.E.W., Peters, A., Chase, J.G., 2011. Phantom elasticity reconstruction with Digital Image Elasto-Tomography. J. Mech. Behav. Biomed. Mater. 4 (8), 1741–1754.

Olson, L.G., Throne, R.D., Nolte, A.J., Crump, A., Griffin, K., Han, T., Iovanac, N., Janssen, T., Jones, M., Ling, X., Samp, M., 2019. An inverse problem approach to stiffness mapping for early detection of breast cancer: tissue phantom experiments. Inverse Probl. Sci. Eng. 27 (7), 1006–1037.

Luo, P., Mei, Y., Kotecha, M., Abbasszadehrad, A., Rabke, S., Garner, G., Goenezen, S., 2018. Characterization of the stiffness distribution in 2D and 3D using boundary deformations – A preliminary study. MRS Commun. 8 (3), 893–902.

Mei, Y., Fulmer, R., Raja, V., Wang, S., Goenezen, S., 2016. Estimating the non-homogeneous elastic modulus distribution from surface deformations. Int. J. Solids Struct. 83, 73–80.

Mei, Y., Wang, S., Shen, X., Rabke, S., Goenezen, S., 2017a. Mechanics based tomography: a preliminary feasibility study. Sensors, Invited Article for Special Issue. Force Press. Based Sensing Med. Appl. 17 (5).

Reddy, J.N., 2005. An Introduction to the Finite Element Method, 3rd ed. McGraw-Hill Education, USA.

Reddy, J.N., 2013. An Introduction to Nonlinear Finite Element Analysis, 2nd ed. Oxford University Press.

Goenezen, S., 2011. Inverse problems in finite elasticity: An application to imaging the nonlinear elastic properties of soft tissues.

Mei, Y., Tajderi, M., Goenezen, S., 2017b. Regularizing biomechanical maps for partially known material propertiese. Int. J. Appl. Mech. 9 (2).

Gupta, S., Parameswaran, V., Sutton, M.A., Shukla, A., 2014. Study of dynamic underwater implosion mechanics using digital image correlation. Proc. Royal Soc. A: Math. Phys. Eng. Sci. 470 (2172), 20140576.

Bonesky, T., 2008. Morozov's discrepancy principle and Tikhonov-type functionals. Inverse Probl. 25 (1), 015015.

Sutton, M.A., Yan, J.H., Tiwari, V., Schreier, H.W., Orteu, J.J., 2008. The effect of out-of-plane motion on 2D and 3D digital image correlation measurements. Opt. Lasers Eng. 46 (10), 746–757.

Luo, P.F., Chao, Y.J., Sutton, M.A., Peters, W.H., 1993. Accurate measurement of three-dimensional deformations in deformable and rigid bodies using computer vision. Exp. Mech. 33 (2), 123–132.

Solav, D., Moerman, K.M., Jaeger, A.M., Genovese, K., Herr, H.M., 2018. MultiDIC: an open-source toolbox for multi-view 3D digital image correlation. IEEE Access. 6, 30520–30535.